Microstructural evolution and oxidation behavior of 13Cr-ODS steel tube after exposure at 1200 °C

Nuclear Materials and Energy 47 (2026) 102142

Contents lists available at ScienceDirect

Nuclear Materials and Energy

journal homepage: www.elsevier.com/locate/nme

Microstructural evolution and oxidation behavior of 13Cr-ODS steel tube after exposure at 1200 °C

Xiao Qin [a,b], Gaoyong Lin [a], Yu Cao [b], Huiqun Liu [a,*]

[a] School of Materials Science and Engineering, Central South University, Changsha 410083, PR China
[b] Department of Industrial and Materials Science, Chalmers University of Technology, Gothenburg 41296, Sweden

ARTICLE INFO

Keywords:
Microstructure
13Cr-ODSsteel
Oxidation
Thermal exposure

ABSTRACT

Oxide dispersion-strengthened (ODS) steels are attractive candidates for fuel cladding in Generation IV reactors, due to their exceptional radiation resistance and high-temperature stability. This study investigates the microstructural evolution and oxidation kinetics of industrial pilgered 13Cr-ODS steel tubes during isothermal exposure at 1200 °C. Results indicate that the initially deformed, fibrous grains undergo partial recrystallization and significant grain coarsening after 20 h of exposure. This structural degradation is driven by a compromise between high stored deformation energy and Zener pinning from nano-oxides. High-temperature oxidation follows a transition from linear to parabolic growth kinetics, with a rate constant of approximately $K_p = 54.32\ mg^2\ cm^{-4}\ min^{-1}$. Characterization reveals a non-protective bilayer oxide scale consisting of an outer Fe_3O_4 layer and a porous inner $FeCr_2O_4$ spinel layer.

1. Introduction

Oxide dispersion-strengthened (ODS) steels are considered the promising candidates for Generation IV fission reactors [1]. In ODS steels, high density of nano-oxides (NO) gives it ultra-fine grain size and high strength (>1 GPa), superior radiation swelling resistance [2], and exceptional thermal stability [3] creep properties [4,5]. Typically, these steels contain 9–16% Cr to enhance oxidation resistance, utilizing low-activation alloying elements such as W, V, and Ti to replace Mo, Nb with long-lived radioactivity in conventional steels [6]. The added NO particles stabilize the microstructure by pinning dislocations and grain boundaries, thereby hindering recovery and creep [7].

The microstructure of ODS steel is inherently linked to its thermo-mechanical processing history. These steels are produced via mechanical alloying of powders followed by high temperature consolidation. Although a variety of consolidation methods [8–10] have been explored to produce ODS steels, including hot extrusion [8], hot isostatic pressing [9] and spark plasma sintering [10], the components produced are mostly simple geometries of rectangular bars or cylindrical rods. The geometries of critical components in real applications differ significantly from the initial geometries generated by consolidation. For example, fuel claddings require converting simple rod into thin-walled seamless tubes. Pilgering has proven to be a viable and efficient processing method to date. Recent related reports [11,12] have successfully demonstrated the ability to produce full-scale thin-walled ODS steel cladding.

The ODS steel cladding acts as a critical safety barrier, separating radioactive fuel from coolant. However, under loss-of-coolant accident (LOCA) conditions, the cladding temperature rises sharply to 1200 °C, posing a significant risk of degradation [13]. Thermal exposure temperature and duration are known to be key factors affecting the microstructure and oxidation behavior. Schneibel et al. [14] reported that after annealing at 1000 °C for 30 h, the grains of 14YWT (Fe-14Cr-3 W-0.4Ti-0.25Y_2O_3) remained stable at submicron size, but the porosity increased. Furthermore, the high temperature stability of 14YWT depended on the distribution of nanoparticles. High-density Y-Ti-O-rich nano-oxides (<5 nm) led to Zener pinning of grain boundaries and increased the recrystallization temperature. The dissolution-reprecipitation mechanism of NO triggered abnormal grain growth [7]. Studies on MA957 (Fe-14Cr-1Ti-0.3Mo-0.25Y_2O_3) had also noted that aging at 1300 °C for 24 h, the size of (Y,Ti,O)-rich oxide particles increased from 2.4 nm to 9.2 nm and the number density decreased from $\sim 2 \times 10^{24}\ m^{-3}$ to $\sim 8 \times 10^{22}\ m^{-3}$[15]. Regarding oxidation, dispersed Y_2O_3 improved oxidation resistance at 900 °C due to the reactive element effect, though alloys with 13%Cr-ODS alloys might fail after prolonging to 7000 h, while oxidation rate increased significantly with

* Corresponding author.
E-mail address: liuhuiqun@csu.edu.cn (H. Liu).

https://doi.org/10.1016/j.nme.2026.102142
Received 12 March 2026; Received in revised form 26 April 2026; Accepted 15 May 2026
Available online 19 May 2026

exposure to air at 1000 °C and 1100 °C [16].

However, most existing literature focuses on initially consolidated samples, leaving a gap in the research regarding ODS steel tubes with complex thermomechanical histories. Pilgered ODS steel cladding possesses a heterogeneous microstructure and defects such as porosity and component segregation. These tubes exhibit high dislocation density ($\sim 10^{15}$ m^{-2}) and stored deformation energy [17], which provides a strong driving force for recrystallization. This creates a state of microstructural instability when balanced against Zener pinning of NO particles. Additionally, porosity and deformed structure enhance diffusion and oxidation, while component segregation may lead to selective oxidation. It would be very interesting to study the stability of the pilgered 13Cr-ODS steel tubes in thermal exposure environments.

This study investigated the microstructure and oxidation behavior of industrial pilgered 13Cr-ODS steel tubes during isothermal exposure at 1200 °C. Electron microscopies (SEM, TEM) were used to characterize microstructural and oxide layer evolution, while XPS, XRD, EBSD and EDS were used to analyze oxide chemistry, phase and compositions. Oxidation kinetics were evaluated by weight gain. Correlating microstructural evolution with oxidation behavior aims to elucidate the high-temperature oxidation behavior of pilgered 13Cr-ODS steel tubes.

2. Experimental procedures

2.1. Materials and methods

The 13Cr-ODS steel (Fe-13Cr-2 W-0.4Ti-0.2Si-0.1 V-0.3Mn + $0.3Y_2O_3$ in wt.%) investigated in this work was manufactured by advanced powder metallurgy. It was designed to combine ultra-fine grains and high creep strength by maximizing the number density of nanoscale (Y,Ti,O) precipitates throughout the microstructure. Mechanical alloying (MA) was carried out using a planetary ball mill (MITR Instruments), in which pre-alloyed powder was milled with 0.3 wt% Y_2O_3 under a high-purity argon atmosphere The MA powder was encapsulated in a carbon steel can and degassed under vacuum at 500 °C for 4 h. Consolidation was then performed via hot isostatic pressing (HIP) at 1150 °C and 150 MPa for 2 h, resulting in bulk ODS steel. The as-received 13Cr-ODS steel tubes were fabricated by warm pilgering at 650 °C with a reduction of 40%. The detailed fabrication process has been described elsewhere [11]. Specimens were sectioned from a tube (25 mm outer diameter, 1.8 mm wall thickness) into several square segments with dimensions of 10 × 10 × 1.8 mm (width × length × thickness). To assess microstructural stability while minimizing oxidation, a subset of them was isothermally exposed at 1200 °C for up to 20 h in an Ar-protected ceramic tube furnace. To investigate oxidation behavior, remaining specimens were placed in a muffle furnace preheated to 1200 °C and exposed to air for up to 10 h. Following exposure, all samples were air-cooled to room temperature. The weight change of oxidized samples was measured using a precision balance (0.1 mg). To ensure reproducibility, the reported data represents the average of two parallel specimens, with error bars indicating the average deviation from the mean value.

2.2. Microstructural characterization

To characterize the microstructure, the tube was sectioned longitudinally and metallographically ground and polished with final colloidal silica suspension (0.06 μm). The phase identification was performed via X-ray diffraction (XRD), using a Bruker D8 Discover diffractometer (Cu-K_α radiation) operating at 40 kV and 40 mA. The chemical state of oxide surfaces was analyzed by X-ray photoelectron spectroscopy (XPS) using PHI 5000 Versa Probe III photoelectron spectrometer with Al K_α excitation ($h\gamma = 1486.6$ eV). For XPS narrow spectrum analysis, calibration was performed with reference to the C1s peak at 284.8 eV. Microstructural morphology and crystallographic orientation were analyzed using a TESCAN MIRA3 scanning electron microscope (SEM) equipped with an Oxford C-nano electron backscatter diffraction (EBSD) detector. EBSD data were collected at an accelerating voltage of 20 kV, a working distance of 14 mm, and step sizes ranging from 0.1 to 0.3 μm. EBSD data post-processing was conducted using Tango plugin in HKL* Channel 5 software to generate inverse pole figure (IPF), recrystallization fraction (RF), geometrically necessary dislocation (GND) and phase maps. Additionally, the cross-sectional morphology and elemental distribution of oxide layers were characterized using a LEO-1550 SEM equipped with energy dispersive X-ray spectroscopy (EDS). Detailed observation of nanoparticles and dislocations substructures were performed using a FEI Tecnai F30 transmission electron microscopy (TEM) operated at 300 kV. TEM foils were prepared using a dual-jet electropolisher (Struers, TenuPol-5, Denmark) in an electrolyte containing perchloric acid and methanol (1:9) at temperatures below –20 °C and a voltage range of 30 V.

Nanoparticle quantification was performed using Image-J Fiji software. To ensure accuracy, a machine- learning based approach was employed via the Trainable Weka Segmentation plugin to differentiate nanoparticles from the matrix background. After classification, the grayscale images were converted to binary (black and white) to simplify analysis. The “Analyze Particles” function was used to calculate the number density, equivalent circular diameter and size distribution of nanoparticles.

3. Results

3.1. Microstructure of as-received 13Cr-ODS steel tube

The microstructure of the 13Cr-ODS pilgered tube, characterized using backscattered electrons (BSE) and EBSD, is presented in Fig. 1. The BSE image in Fig. 1a reveals a distinct fibrous structure with grains significantly elongated along the pilgering direction. Isolated porosity, a common defect in powder metallurgy resulting from localized insufficient mechanical alloying or incomplete thermal consolidation, is marked by the white arrow. High-magnification image and corresponding elemental map (inset of Fig. 1b) confirm the presence of Cr-rich regions. These banded Cr-rich phases appear fragmented, likely a consequence of the severe plastic deformation during pilgering acting on the chemical inhomogeneities of mixed powder after possible inadequate MA conditions. The crystallographic orientation and grain morphology were further analyzed using EBSD (Fig. 1c). The inverse pole figure (IPF) map relative to the normal direction (ND) shows a predominance of $< 111 >$//ND oriented grains. Within these deformed grains, orientation gradients and a high density of low-angle grain boundaries (LAGB, indicated by red lines) are evident, signifying high stored strain energy. When referenced to rolling (pilgering) direction (RD), the inset of Fig. 1c, reveals a strong $< 110 >$//RD fiber. This orientation is characteristic of body-centered cubic (BCC) materials subjected to the plastic deformation resulting from the e preferential activation of the $\{110\} < 111 >$ slip system. Quantification of EBSD analysis indicates that the recrystallized grains account for approximately 8.3% of the analyzed area, confirming that the microstructure remains primarily in a deformed state. The grain size distribution, selected from a representative mid-thickness region, is shown in Fig. 1d. The as-pilgered steel tube exhibits an average grain size of 1.2 μm. This ultra-fine grain structure provides grain boundary strengthening, as evidenced by the Vickers hardness of 320 ± 6.7 HV1measured on the tube cross-section. Compared to a similar 13Cr-ODS (Fe-13Cr-2 W-0.6Zr-0.4Ti + 0.3 Y_2O_3) steel tube reported by Zhang et al. [11], which possessed a grain size of approximately 2 μm and a tensile strength of 908 MPa.The finer grain structure achieved here suggests superior potential for high-temperature mechanical performance.

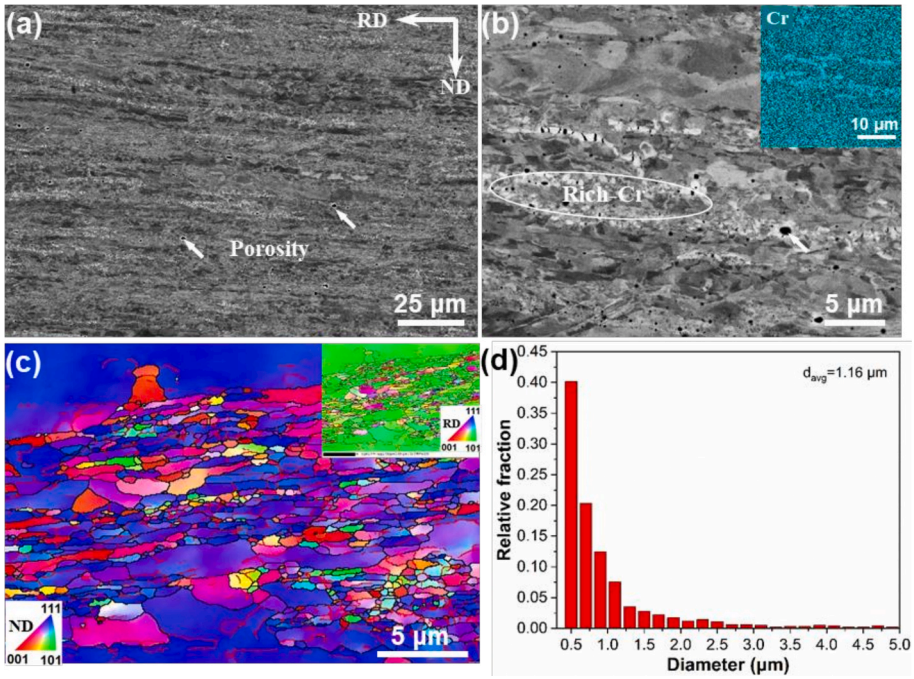

Fig. 1. (a) (b) Backscattered electrons (BSE) images, (c) Inverse pole figure (IPF) map and (d) Grain size histogram of as-received 13Cr-ODS steel tube.

3.2. High-temperature microstructure

3.2.1. Grain microstructure

The BSE images of 13Cr-ODS steel tube after exposure to 1200 °C for 20 h are shown in Fig. 2. Compared to the as-received condition, the thermal exposure induced grain coarsening and partial recrystallization. A heterogeneous microstructure consisting of lamellar deformed grains and coarse equiaxed grains are observed in Fig. 2a, indicating the inadequate dispersion morphology of oxide particles in the material used in this study. This transition from lamellar grains to recrystallized grains occurs primarily in the rolling (pilgering) direction. This indicates a longitudinal gradient microstructural inhomogeneity, reflecting variations in stored deformation energy and localized recrystallization kinetics introduced during the pilgering process. Interestingly, this transition is non-periodic along the longitudinal axis of the tube, suggesting that while the pilgering process induces high deformation, the subsequent recrystallization at 1200 °C is governed by stochastic fluctuations in nanoparticle number density and stored energy. A multimodal grain structure is further detailed in Fig. 2b, where elongated regions coexist with coarse "bamboo-like" recrystallized grains and residual nano-grains. This distribution is governed by the the localized balance between deformation-induced driving forces and the pinning pressure exerted by nanoparticles. The high-magnification images (Fig. 2c) reveal a high-density of white nanoparticles dispersed within the elongated grains. The critical role of these precipitates in stabilizing the microstructure is demonstrated in Fig. 2d. In the upper region where nanoparticles density is low, grains are larger than 2 μm. Conversely, in lower regions with high-density nanoparticles, subgrain boundaries remain poorly defined and effectively pinned, inhibiting grain growth. The localized absence of Zener pinning leads to abnormal grain growth, with some grains reaching sizes of 20 μm (Fig. 2e). These nanoparticles, previously identified as nano-oxides (Y,Ti,O) [18], are known to hinder

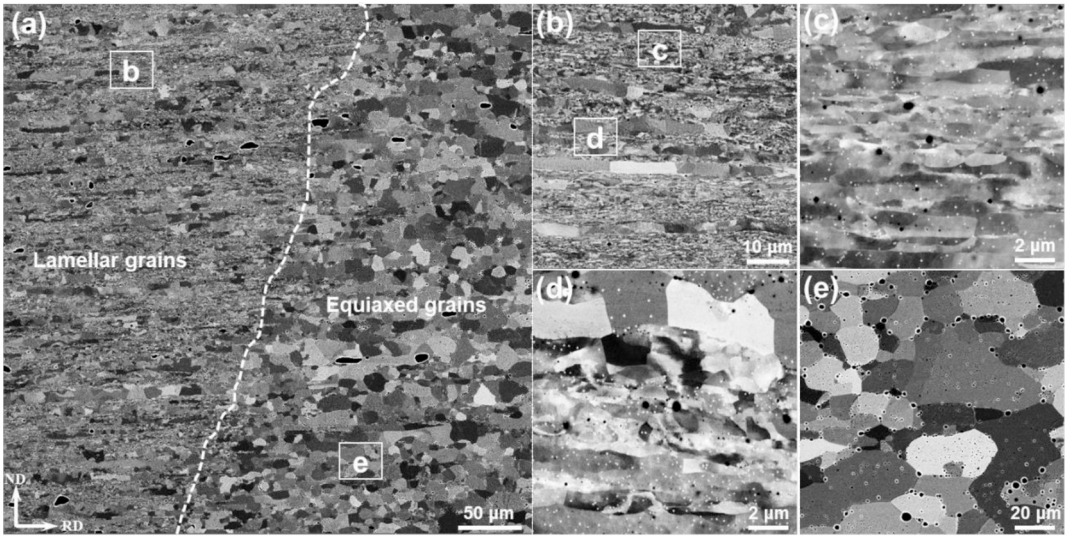

Fig. 2. BSE images of 13Cr-ODS steel tube isothermal at 1200 °C for 20 h. (a) Low magnification image, (b-e) High magnification images.

the migration of sub-grain boundaries and dislocations, thereby significantly elevating the recrystallization temperature of 13Cr-ODS steel. Furthermore, Fig. 2e reveals the presence of micropores, ranging from several hundred nanometers to several micrometers, located both at grain boundaries and within grains interiors. The observed porosity is likely associated with the coalescence and expansion of trapped gases (Ar) during high-temperature annealing [14]. The porosity increased from 2.39% in the as-received condition to 6.37% after exposure at 1200 °C, suggesting that pore growth is primarily driven by the expansion of pre-existing gas-filled cavities.

The multi-scale structure of the 1200 °C annealed microstructure, characterized by the coexistence of deformed and recrystallized regions, was further investigated using EBSD and TEM (Figs. 3 and 4). Fig. 3 presents IPF, recrystallization fraction (RF) and geometrically necessary dislocation (GND) maps. The IPF maps for both the partial and recrystallized regions reveal strong α-fiber. Notably, the RF maps indicate that α-fiber remains largely unaffected by the progression of recrystallization, maintaining its dominance in both deformed and newly formed equiaxed grains. The GND maps confirm a higher dislocation density within lamellar deformed grains compared to interior of recrystallized grains, consistent with the consumption of stored energy during boundary migration. However, the observation that α-fiber orientation is ubiquitous across all grain scales suggests that crystallographic texture is not the primary driver for the observed multiscale heterogeneity. Instead, the morphology of the lamellar grains appears to correlate with the banded, Cr-rich regions identified in Fig. 1b, suggesting that chemical banding, rather than orientation, governs the localized resistance to recrystallization.

The exceptional thermal stability of the 13Cr-ODS steel after 20 h of exposure at 1200 °C is further elucidated by the TEM bright-field images in Fig. 4. As shown in Fig. 4a, the lamellar grains with a width of about 300 nm due to extreme pilgering, remain stable. This stability is tied to a bimodal microstructural distribution (Fig. 4b) consisting of fine grains with high dislocation densities and larger grains with lower dislocation densities. The coexistence of dense dislocation entanglements in deformed regions alongside relatively "clean" recovered grains highlights the inhomogeneity of stored deformation energy across the microstructure. At higher magnification (Fig. 4c), dislocation pile-ups are observed at both grain boundaries and surrounding individual nanoparticles. This provides direct evidence of Zener pinning, where the fine nanoparticles hinder dislocation annihilation and motion, even at $0.8T_m$ (melting temperatures). In partially recrystallized regions (Fig. 4d), dislocation entanglements persist, while "bamboo-like" recrystallized bands are often surrounded by lamellar grains that still retain their high-density dislocation substructures (Fig. 4e). The contrast in dislocation density is further quantified in Fig. 4f, where recrystallized grains exhibit lower densities compared to their deformed grains. Interestingly, within $< 111 >$ -oriented deformed grains, dislocations have rearranged into dislocation cells. A distinct correlation was observed between grain morphology and internal strain: coarse grains with low dislocation density exhibited straight, high-angle boundaries, whereas fine polygonal grains retained high dislocation densities due to the pinning effect of agglomerated nanoparticles. These observations align with studies [3–5,19], confirming that nanoparticle-dislocation interaction is the primary mechanism delaying recrystallization and maintaining the fine grain structure at extreme temperature.

3.2.2. Nano oxides

The spatial distribution and size evolution of nano-oxides within typical grains morphologies were quantified using STEM-BF images and statistical histograms (Fig. 5). In the fine equiaxed grains (Fig. 5a), nano-oxides are randomly and densely distributed. Statistical analysis (Fig. 5d) reveals an average particle size of about 7.5 nm with a high number density of 6.03×10^{14} m^{-2}. In the elongated coarse grains, nano-oxides are found at the grain boundaries (Fig. 5b), exhibiting a lager average particle size of 10.6 nm and a reduced number density. The correlation between precipitate characteristics and matrix morphology is further emphasized in Fig. 5c, which captures the extreme disparity in nano-oxide distribution between coarse and fine grains. In coarse grains, nano-oxides are nearly absent, whereas they remain highly dispersed within the adjacent fine grains. In these coarsened regions, the average particle size increases to about 18.7 nm, while the number density drops by an order of magnitude to 2.33×10^{13} m^{-2}. These findings indicate that the localized stability of the microstructure is dictated by the Zener pinning pressure, which is a function of the particle size and volume fraction. The inhomogeneity of the nano-oxide distribution, driven by localized coarsening and reduction in number density, is the primary factor governing the observed grain size heterogeneity. Where nano-oxides coarsen or deplete, the pinning force is insufficient to counteract the driving force for grain boundary migration, leading to the formation of coarsening, nearly defect-free grains. It is noteworthy that the number density of oxide particles in the 13Cr-ODS steel prepared in this study is one to two orders of magnitude lower than that reported for typical ODS steels [15]. This suggests that the current processing conditions require further optimization to achieve a fine and homogeneous dispersion of oxide nanoparticles.

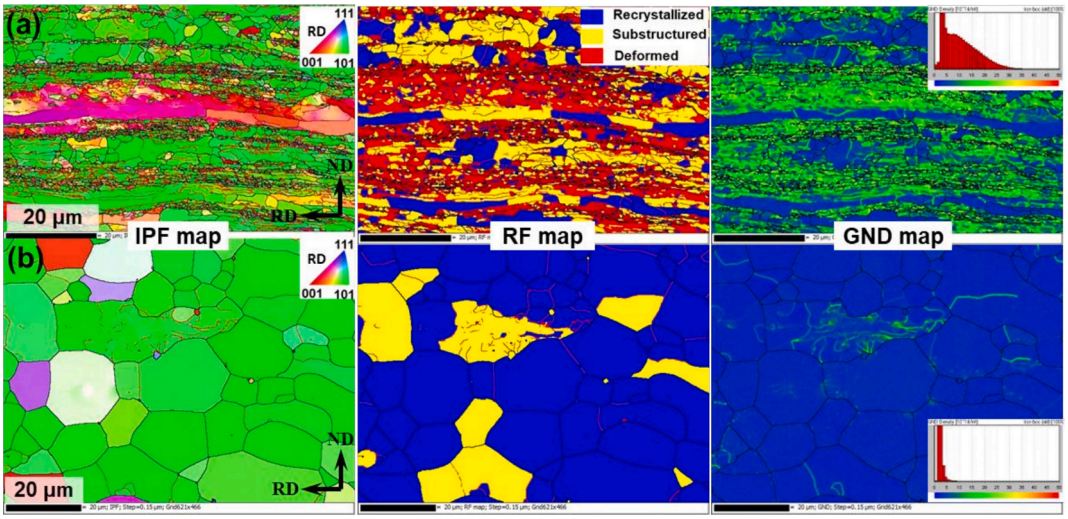

Fig. 3. EBSD results of (a) partially recrystallized and (b) recrystallized 13Cr-ODS steel tube.

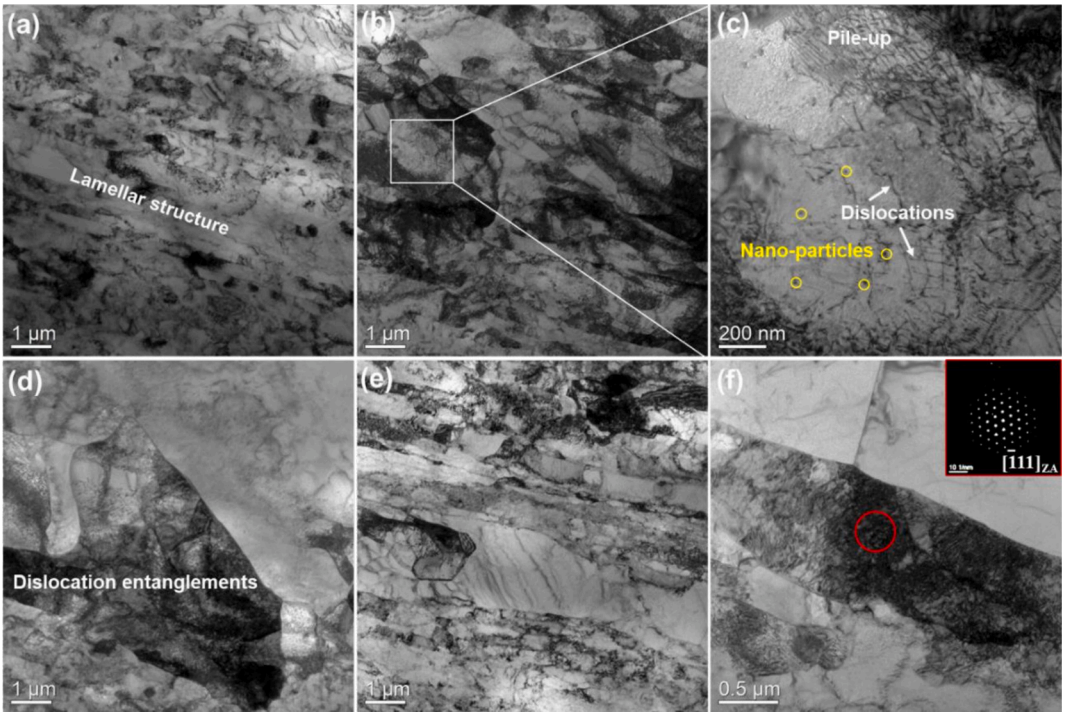

Fig. 4. TEM-BF images of 13Cr-ODS steel tube after exposure to 1200 °C for 20 h. (a) Deformed grains, (b,c) Recovered grains, (d-f) Partially recrystallized grains.

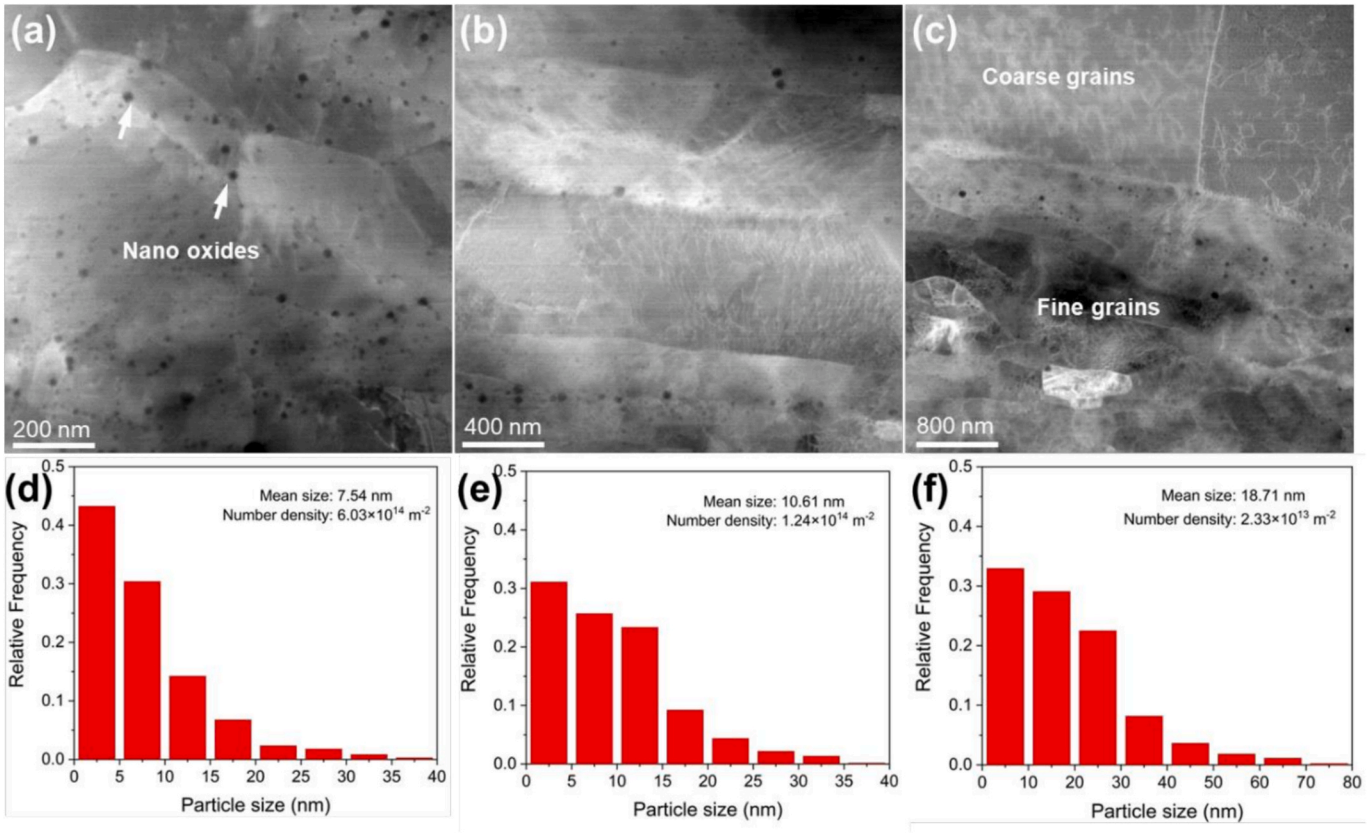

Fig. 5. STEM-BF images (a-c) and statistical nano-oxide size histogram (d-f) of 13Cr-ODS steel exposed at 1200 °C for 20 h. (a,d) fine grains (b,e) coarse grains, (c,f) fine grains/coarse grains.

3.3. Oxidation behavior

3.3.1. Oxidation kinetics

The oxidation behavior of 13Cr-ODS steel was investigated through isothermal exposure at 1200 °C for up to 10 h. The weight gain per unit area as a function of oxidation time is presented in Fig. 6a. A sharp increase in oxidation weight gain means poor oxidation resistance of the alloy. The weight gain rate showed a linear growth in the initial stage of oxidation and a parabolic growth in the later stage. The parabolic growth rate follows Wagner's oxidation theory [20], which assumes the growth rate of oxide layers is primarily controlled by the solid-state diffusion of ions through the forming scale. The oxidation kinetics can be described by the following parabolic relationship [20].

$$(\Delta W/A)^n = Kp^t \quad (1)$$

Where $\Delta W/A$ is the weight gain per unit area (mg/cm^2), K_p is the parabolic rate constant, n is the oxidation rate exponent and t is the oxidation time. By fitting the experimental data, the value of n was determined to be to 2.016≈2, the kinetics strictly follow a parabolic growth law. Fig. 6b shows the square of the weight gain plotted against oxidation time, showing a strong liner correlation (R^2) with parabolic kinetics. Following 10 h of exposure at 1200 °C, the calculated parabolic rate constant (K_p) for 13Cr-ODS steel was ~54.32 $mg^2\ cm^{-4}\ min^{-1}$.

3.3.2. Characteristics of the oxide layer

XPS spectra were recorded to characterize the surface chemistry of 13Cr-ODS steel in both as-received and oxidized surface (Fig. 7). The survey spectrum of the as-received surface (Fig. 7a) shows that signals for Mn, V, Ti, Si, W, and Y were below the reliable detection threshold. The presence of carbon peak (C1s) peak is attributed to adventitious organic species absorbed from the atmosphere, while the abnormal Cu signal is likely due to impurities. Upon thermal exposure at 1200 °C for 1 min, signals for Y, W, Ti, Mn, and V became visible, indicating surface enrichment of these alloying elements. The concurrent increase in oxygen peak (O1s) and Cr peak (Cr2p3) intensity indicates the rapid formation of an oxide scale. Detailed narrow spectra are provided in Fig. 7b. In the as-received state, the surface consists of minor amounts of (Cr, Fe) oxides alongside metallic Fe. Following the 1-min exposure, the metallic Fe peak disappears, signaling the growth of an oxide layer thicker than the XPS escape depth. This oxidized surface is dominated by Fe^{3+} and Cr^{3+}. Furthermore, while Y, Ti, and W were undetectable in as-received state, they exhibit strong Y^{3+}, Ti^{4+}, and W^{6+} peaks after exposure. The emergence of these high-valence states underscores the high oxygen affinity of these reactive elements, leading to the formation of stable, complex oxides at the outermost surface during the early stages of oxidation.

The phase evolution of the 13Cr-ODS steel before and after thermal exposure is characterized by the XRD patterns presented in Fig. 8. In the as-received state, the diffraction pattern is dominated by the (Cr, Fe) ferrite phase, with no detectable oxide reflections. Notably, a distinct tungsten (W) diffraction peak was identified, indicating component segregation. Following exposure at 1200 °C for 20 min, the diffraction patterns undergo a transition. The intensity of the ferrite peaks is markedly attenuated, while strong reflections corresponding to spinel-type oxides, specifically magnetite (Fe_3O_4) and iron-chromium spinel ($FeCr_2O_4$), emerge. This attenuation of the matrix signal is a direct result of the thickening oxide scale, which increases the X-ray absorption and limits the penetration depth to the underlying steel substrate.

Note that W, V and WC peaks are also found, which indicate that the composition of the samples was inhomogeneous. These results corroborate the "banded" Cr-rich morphology discussed previously, confirming that the initial processing-induced segregation leads to a complex, multi-phase microstructure upon oxidation.

The microstructure and elemental distribution of the oxide layer formed after 20 min of exposure at 1200 °C are shown in Fig. 9. Secondary electron (SE) images reveal a thick dual-layered oxide layer with a total thickness of ~ 35 μm. The oxide layer is comprised of a porous outer layer and a loose inner layer. EDS elemental maps identifies that the outer porous layer as being enriched in O and Cr, with a lower Fe relative to the matrix. The phase map confirms that the outer region consists of a spinel-type $FeCr_2O_4$. IPF further indicates that $FeCr_2O_4$ is composed of randomly oriented, nano-sized grains. The observed porosity within diffusion layer likely represents a complex mixture of $FeCr_2O_4$ and Cr_2O_3 [21]. Notably, Fe-rich regions were observed surrounding the micropores. This localized enrichment suggests a vacancy-diffusion mechanism, wherein the outward flux of Fe ions is not fully compensated by the inward flux of vacancies, potentially lead to Kirkendall-type porosity. The inner oxide layer is rich in Cr, O, Si and W. The region as a black background was not indexed due to unknown crystal structure. Based on literature [22], this inner scale likely consists of a complex mixture of SiO_2, Cr_2O_3 and WO_3. In contrast to the randomly oriented oxide, the underlying steel matrix maintains a strong α-fiber, consistent with the bulk EBSD results shown in Fig. 3.

Figs. 10 and 11 reveals the cross-sectional SE images and EDS elemental maps of the oxide layers after 60 min and 120 min exposure, respectively. A significant increase in scale thickness was observed as a function of exposure time. Notably, SE images in Fig. 10 reveal a high density of micropores within the matrix adjacent to the oxide/matrix interface, which are attributed to the Kirkendall effect during oxidation [23]. Compared to the dense bulk matrix, this interconnected pore

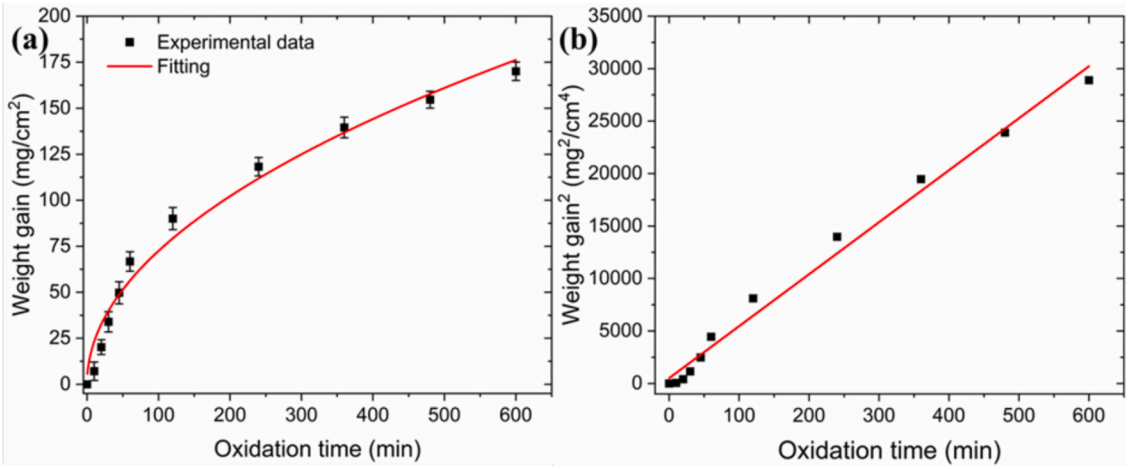

Fig. 6. (a) Weight gain versus oxidation time curve and (b) linear fit of the square of weight gain versus oxidation time of 13Cr-ODS steel exposure at 1200 °C for 10 h, confirming the parabolic nature of oxidation curve.

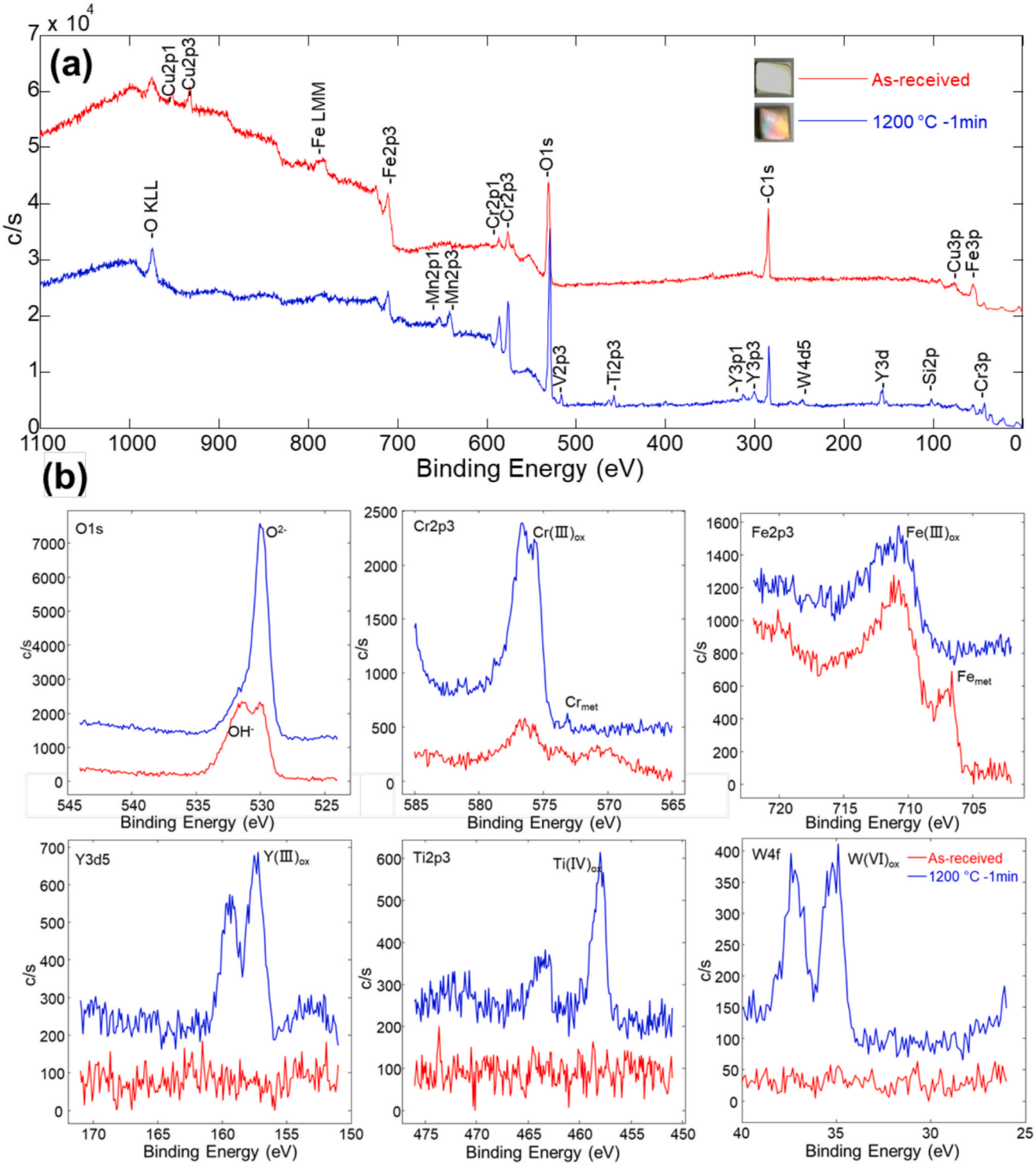

Fig. 7. XPS survey (a) and narrow (b) spectra of the surface of 13Cr-ODS steel after exposure at 1200 °C for 1 min.

network provides a lower resistance pathway for oxygen ingress, thereby facilitating internal oxidation and accelerating the growth of oxide scale. EDS elemental mapping of the 1200 °C-60 min specimen indicates an oxide layer enriched in O and Cr with depleted Fe levels. The continued enrichment of Si at the interface suggests a persistent, albeit localized, attempt to form a SiO_2 diffusion barrier. However, by 120 min (Fig. 11), the oxide scale reaches a thickness of approximately 500 μm and develops a distinct bilayer architecture. The outer layer is heavily fragmented and composed primarily of Fe and O with negligible Cr, identified as magnetite (Fe_3O_4). The inner layer remains a porous structure enriched in Cr and O, corresponding to the $FeCr_2O_4$ spinel identified in previous XRD and EBSD analyses. In high chromium steels exposed to high temperatures or oxidizing environments, Fe_3O_4 typically forms the outermost layer, while Cr-rich oxides develop internally due to lower oxygen partial pressures at the sacle/substrate interface [24,25]. While a dense outer Fe_3O_4 can theoretically act as a diffusion barrier, its effectiveness is compromised here by its fragmented state and the underlying porosity of the $FeCr_2O_4$ sub-scale. This porous morphology facilitates the rapid penetration of oxygen, leading to the observed exacerbation of internal oxidation and the rapid consumption

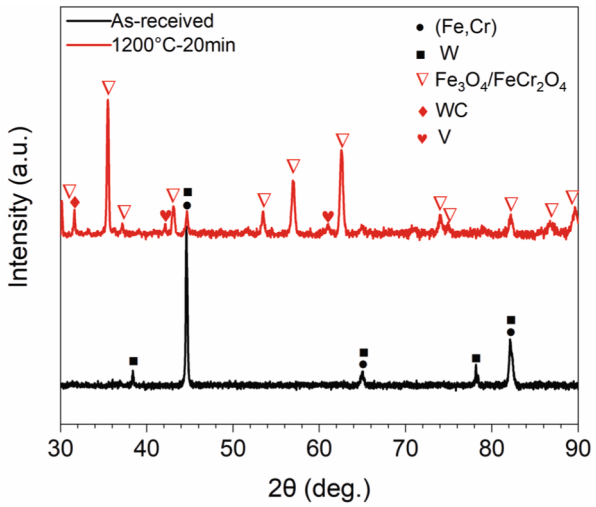

Fig. 8. XRD patterns of as-received 13Cr-ODS steel and after exposure at 1200 °C for 20 min.

of the ODS steel substrate.

To observe the surface morphology evolution, the as-received sample was mechanically polished and then subjected to 1200 °C thermal exposure. In the as-received condition (Fig. 12a, the polished surface exhibited fibrous grain structure characteristic of high-reduction pilgering, with grain elongated along the rolling direction. Following 10 h of thermal exposure at 1200 °C, significant surface cracking is observed in Fig. 12b. This cracking is usually caused by volume expansion associated with the conversion of metal substrate into a thick oxide scale. The resulting in high internal stress at the matrix/oxide interface, combined with the inherent brittleness of the complex spinel oxides at these temperatures, lead to a loss of interfacial adhesion. As shown in Fig. 12c, the resulting oxidation debris exhibits sharp, angular features characteristic of brittle fracture. The transition from a continuous scale to fragmented debris indicates that the formed oxides are non-protective and prone to spallation.

4. Discussion

The 13Cr-ODS steel was designed to introduce high density nanoparticles to enhance microstructural thermal stability under extreme conditions. The as-received 13Cr-ODS steel tube was processed via warm pilgering, resulting in a heavily deformed, fibrous grain structure. Owing to Zener pinning effect of NO, the recrystallization temperature of ODS steels has been reported to reach up to 0.9 T_m [26]. This is significantly higher than the recrystallization threshold of conventional alloys, which at typically occurs at approximately 0.5 T_m [27]. In the context of the generation-IV supercritical water-cooled reactor, the normal operating temperature is ~ 550 °C. At this temperature, the 13Cr-ODS steel maintains its deformed state without significant

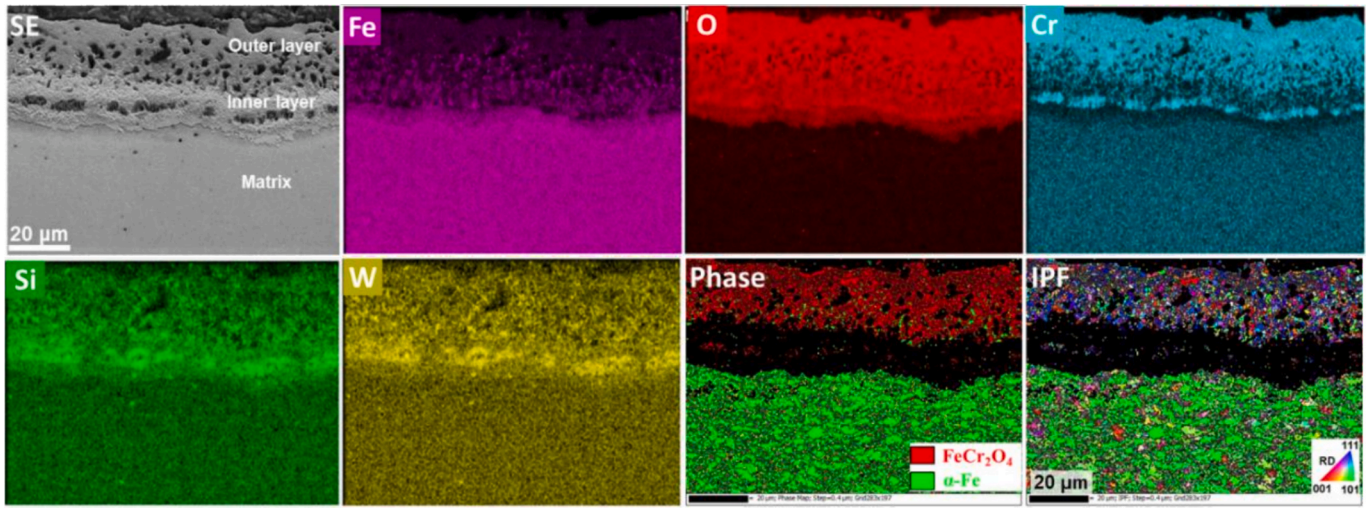

Fig. 9. The cross-sectional SE images, EDS, phase and IPF maps of 13Cr-ODS steel exposed at 1200 °C for 20 min.

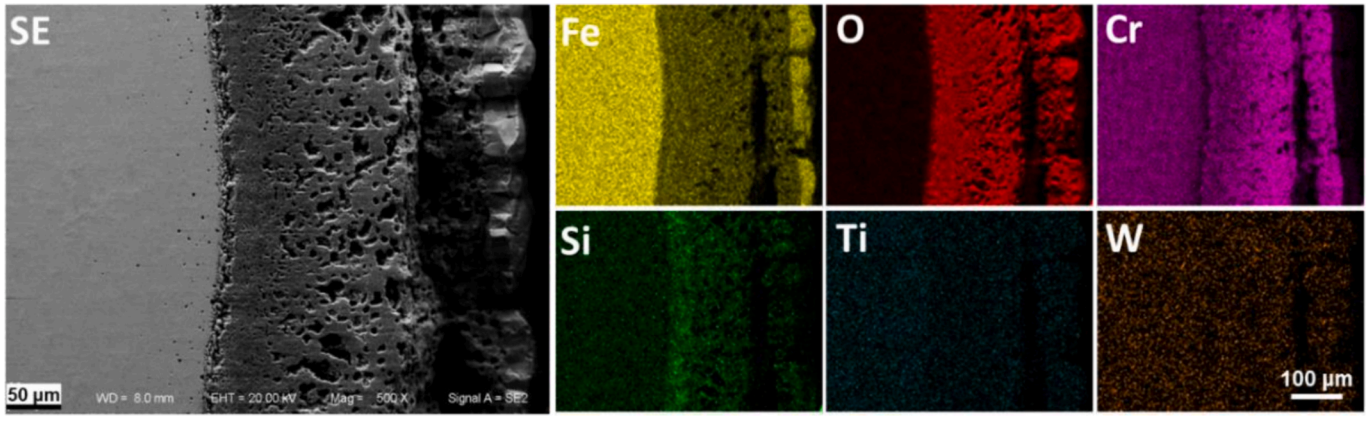

Fig. 10. The cross-sectional SE images and EDS elemental maps of 13Cr-ODS steel exposed at 1200 °C for 60 min.

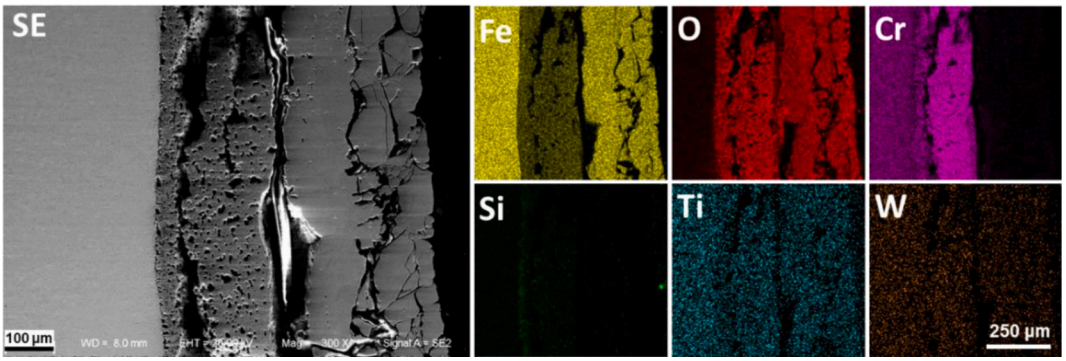

Fig. 11. The cross-sectional SE images and EDS elemental maps of 13Cr-ODS steel exposed at 1200 °C for 120 min.

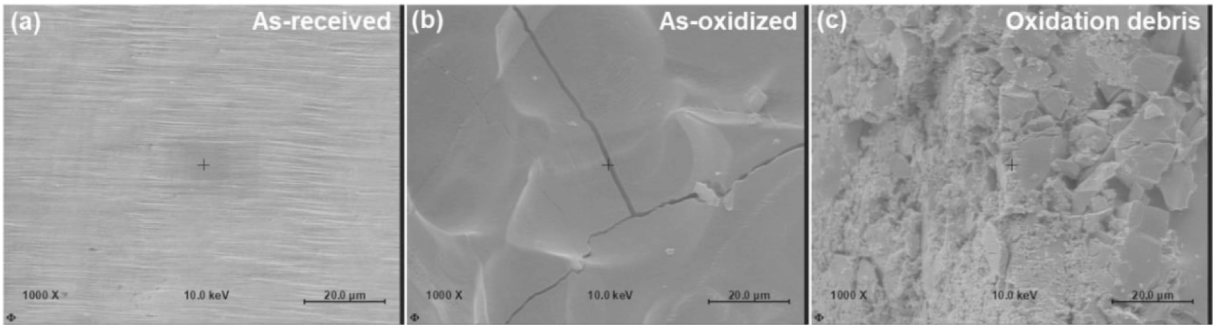

Fig. 12. Surface morphology of (a) as-received 13Cr-ODS steel tube with polishing and after (b, c) exposure at 1200 °C for 10 h.

recovery or recrystallization, ensuring high creep resistance. However, during a LOCA, cladding temperature can rise sharply to 1200 °C due to decay heat accumulation. Under such extreme off-normal conditions, the cladding is subjected to simultaneous risks of rapid microstructural recrystallization and accelerated high-temperature oxidation. Understanding the stability of the 13Cr-ODS steel at 1200 °C is therefore critical for assessing the safety and structural integrity of the fuel cladding during accidental transients.

4.1. Thermal recrystallization

Microstructural observations and hardness measurements indicate that thermal exposure 1200 °C for 20 h induces partial recrystallization of 13Cr-ODS steel tube, as shown in Fig. 2. The recrystallization is the result of the compromise between stored deformation energy and Zener pinning pressure of nanoparticles.

The grain boundary velocity (ν) in the 13Cr-ODS steel is a function of boundary mobility (M) and the net driving force (ΔP), as described by the following equation [28].

$$\nu = \mathrm{M} \times \Delta \mathrm{P} = \mathrm{M}_0 \exp\left(-Q/RT\right) \times \left(P_s + P_c - P_z\right) \tag{2}$$

where M is the boundary mobility between the recrystallized nucleus and the surrounding deformed matrix, P_s is the stored dislocation energy, P_c is the grain boundary curvature pressure, and P_z is the Zener pinning pressure.

The stored dislocations energy can be expressed as [28]:

$$P_s = 1/2Gb^2\rho \tag{3}$$

where G is the shear modulus (~ 81 GPa for 14YWT alloys [6]), b is the Burgers vector length (~2.5Å), and ρ is the dislocation density (4.61×10^{14} m^{-2}, determined via CMWP fitting [29]). P_s is calculated to be ~ 1.17 MPa.

The volume average grain boundary pressure is defined [30].

$$P_c = 2\gamma/d \tag{4}$$

where γ is the high-angle grain boundary energy (~1 J/m^2 [31]), d is the initial grain size ~1.2 μm. Thus, P_c is calculated as ~1.67 MPa.

The Zener pinning pressure can be expressed as [32].

$$P_z = 3f\gamma/2r \tag{5}$$

Where f is the particle volume fraction, and r is the average particle radius. Based on TEM analysis, the f and r of particles are 2.03%, 10 nm, respectively. The calculated P_z is 3.05 MPa. The calculated ΔP = -0.21 MPa. A negative ΔP means that the Zener pinning pressure exceeds the driving force for recrystallization, thereby restricting grain boundary migration. This explains the high fraction of stable deformed structures observed in Figs. 2-4. However, the local heterogeneity of the microstructure allows for the partial recrystallization observed. Specifically, variations in nanoparticle density and localized "hot spots" of high dislocation density create regions where $P_s > P_z$. In areas where nanoparticles coarse or deplete (as seen in Fig. 5b & c), P_z drops significantly, allowing boundaries to break free and consume the deformed matrix. The consequences of this recrystallization are reflected in the mechanical properties: the hardness of the coarse recrystallized grains dropped to 160 HV1, exactly half that of the as-received state (320 HV1). This degradation underscores the risk posed to cladding structural integrity during a 1200 °C thermal transient, such as a LOCA.

4.2. High temperature oxidation

The oxidation of 13Cr-ODS steel tube at 1200 °C is characterized by a transition from surface-reaction-limited to diffusion-limited kinetics. As shown in Fig. 6a, the initial linear weight gain indicates that the substrate is directly exposed to the atmosphere, where oxygen is readily available and the reaction rate is not yet restricted by a physical barrier. As continuous oxide film develops, the mechanism shifts to parabolic growth. At this stage, further oxidation is governed by the solid-state

diffusion of metal cations or oxygen anions through the thickening scale, resulting in a mass gain that is proportional to the square root of time (Fig. 6b). The sequence of oxide formation is dictated by the standard Gibbs free energy of formation (ΔG_f^O), as illustrated by the Ellingham diagram [33]. Elements with more negative ΔG_f^O values exhibit a higher thermodynamic affinity for oxygen and will oxidize preferentially. XPS analysis (Fig. 7) confirms that in the early stages of oxidation, the surface is enriched with microalloying elements such as Mn, Si, Ti, V, and Y. According to the ΔG_f^O values at 1200 °C (Table 1), these elements oxidize more readily than Fe or Cr. However, these transient oxides are typically discontinuous or highly permeable, failing to provide a robust diffusion barrier. The structural evolution of the scale is a competition between the highly stable Cr_2O_3 and the rapidly growing Fe-based spinels. While ΔG_f^O analysis indicates that Cr_2O_3 is more stable than Fe_3O_4 or $FeCr_2O_4$ (Table 1), its persistence is limited under the experimental conditions.

While Cr_2O_3 initially provides superior oxidation resistance, the high oxygen partial pressure at 1200 °C promotes its further reaction with the outwardly diffusing Fe ions to form the spinel phase $FeCr_2O_4$ [34]. The combination of XRD, SEM-EDS, and EBSD (Figs. 8-11) confirms that the scale eventually thickens into a bilayer dominated by Fe_3O_4 and $FeCr_2O_4$. This indicates that at such extreme temperatures, the Cr reservoir is insufficient to maintain a purely Cr_2O_3 protective layer, leading to the formation of the thicker, more porous spinel-based scale that characterizes the breakaway oxidation regime.

Beyond thermodynamics, the oxidation rate of 13Cr-ODS steel is governed by the kinetics of ionic transport. Microstructural features such as grain boundaries, dislocations, and micropores (Fig. 1) serve as fast diffusion pathways, significantly accelerating the outward migration of metal cations and the inward ingress of oxygen. Crystallographic orientation also plays a decisive role in surface reactivity and ion diffusivity. In BCC metals, the atomic packing density of different planes dictates the oxidation rates. The < 110>//ND texture generally exhibits the slowest oxidation rate due to lower surface reactivity and limited diffusion path [36]. The < 001>//ND and < 111>//ND textures exhibit high oxidation rates due to the high surface energy of the former and the high density of associated dislocations in the latter [37]. The strong < 001>//ND and < 111>//ND textures (Fig. 1c) observed in the pilgered 13Cr-ODS steel tube led to poor oxidation resistance. Most importantly, Cr is the dominant factor controlling the oxidation rate. While Cr ≥ 12% Cr theoretically favors the formation of a protective Cr_2O_3 layer, the high growth rates at 1200 °C demand a rapid flux of Cr to the metal/oxide interface to maintain a continuous film. When the Cr supply cannot keep pace with the oxidation front, Fe-based oxides (Fe_3O_4, $FeCr_2O_4$) begin to form. The bilayer structure observed in Fig. 11 results from the differential diffusion rates of Fe and Cr cations. Fe cations diffuse outward through the scale more rapidly than Cr, reacting at the surface to form the brittle Fe_3O_4 outer layer. This rapid outward flux generates a high concentration of vacancies at the metal/oxide interface. Simultaneously, the slower-diffusing Cr atoms accumulate in the inner region, promoting the formation of the porous $FeCr_2O_4$ spinel. The condensation of these vacancies leads to the extensive internal porosity observed in Figs. 9-11.

In general, for Cr ≥ 12%, the thermodynamics favor the formation of a Cr_2O_3 layer. However, the kinetics require that there is enough Cr at the metal/oxide interface to form a continuous chromium oxide film and maintain protection. At very high temperatures, the oxide growth rate increases, generating significant compressive stresses within the scale that can lead to spallation. Rapid thermal cycling exacerbates this effect by repeatedly expanding and contracting the oxide layer, promoting crack initiation and propagation. Additionally, alloys with lower Cr content may not form a continuous Cr_2O_3 layer. Then, iron oxides (Fe_3O_4, $FeCr_2O_4$) begin to form, reducing the protective effect and accelerating overall oxidation. The SE images in Figs. 9-11 reveal a porous $FeCr_2O_4$ layer, suggesting significant vacancy condensation and the formation of micropores. The eventual cracking and spalling of the oxide scale (Figs. 11-12) can be analyzed using the Pilling-Bedworth Ratio (PBR), which relates the volume of the oxide produced to the volume of the metal consumed [38].

$$PRB = \frac{1}{n} \bullet \frac{M_{ox}/\rho_{ox}}{M_{met}/\rho_{met}} \tag{6}$$

Where: n is the number of metal cations in the oxide formula, M_{ox} is the molar mass of the oxide, ρ_{ox} is the density of the oxide, M_{met} is the molar mass of the metal, ρ_{met} is the density of the metal.

In this study, Fe_3O_4, Cr_2O_3, and $FeCr_2O_4$ showed high PBR (>1) meaning that the oxide volume exceeds that of the consumed metal substrate (Table 2). While a PBR between 1.5 and 2.0 generally promotes adherence by ensuring full surface coverage, the extreme oxidation rate at 1200 °C leads to an excessively rapid volumetric expansion. This expansion is constrained by the rigid metal substrate, generating high internal compressive stresses within the scale and resultant tensile stresses at the oxide/matrix interface. Coupled with the thermal stress arising from a mismatch in thermal expansion coefficients, these forces initiate brittle cracking and spallation, as evidenced in Fig. 12.

The primary motivation for ODS cladding development is to enhance the high-temperature mechanical strength, creep resistance and microstructural stability of fuel cladding. Fig. 6 indicates that the 13Cr-ODS steel exhibits a high oxidation rate, which remains a critical limitation for its application in accident-tolerant fuel (ATF) cladding [39]. A transition from an initial linear regime to parabolic kinetics at later stages is observed. This behavior, together with concurrent microstructural evolution during high-temperature oxidation, such as recovery/recrystallization, coarsening or redistribution of oxide nanoclusters, and modifications at the oxide/matrix interface, suggesting that diffusion pathways evolve with exposure time. Consequently, the oxidation kinetics are not strictly constant, and the derived rate constant should be regarded as an apparent value over the investigated duration. In this work, the 13Cr-ODS steel tube developed an oxide layer approximately 0.5 mm thick after only 2 h at 1200 °C. According to the U.S. Nuclear Regulatory Commission (10 CFR 50.46) [40], the equivalent cladding reacted (ECR) ≤ 17% of the initial wall thickness to maintain structural integrity. This represents an ECR of 27.8% of the 1.8 mm wall thickness, significantly exceeding the safety limit. While the nanoclusters effectively suppressed bulk recrystallization and maintained high-temperature strength, the alloy's K_p was several orders of magnitude higher than that of FeCrAl or SiC (Table 3). The lower Cr content without addition of Al may be the cause of higher oxidation rate. However, high-temperature steam differs from air, and further testing under high-temperature steam conditions is required to rigorously evaluate its applicability to the LOCA scenario.

Table 1
Standard Gibbs free energies for oxide formation of (pure) elements in 13Cr-ODS steel [35].

Metal	Oxide formation reaction	ΔG_f^O for the oxides at 1200 °C, kJ mol^{-1}
Fe	$3Fe + 2O_2 \rightarrow Fe_3O_4$	−609
Cr	$2Cr + 3/2O_2 \rightarrow Cr_2O_3$	−737
Fe,Cr	$FeO + Cr_2O_3 \rightarrow FeCr_2O_4$	−475

Table 2
Some parameters used to calculate PRB of metal oxide.

Metal	Molar mass of metal (g·mol^{-1})	Density of metal (g·cm^{-3})	Metal oxide	Molar mass of metal oxide (g·mol^{-1})	Density of metal oxide (g·cm^{-3})	R
Fe	55.8	7.9	Fe_3O_4	231.5	5.2	2.1
Cr	52.0	7.2	Cr_2O_3	152.0	5.2	2.0
Fe,Cr	159.8	7.5	$FeCr_2O_4$	223.8	5.2	2.0

Table 3
Parabolic rate constant (K_p) of several candidate claddings at 1200 °C [41–44].

Material	13Cr-ODS steel (This work)	9 Cr martensitic steels	FeCrAl (Fe–13Cr–4.5Al)	SiC
K_p ($mg^2 \cdot cm^{-4} \cdot min^{-1}$)	54.3	100–150	<2.1	$<10^{-3}$

5. Conclusion

The 13Cr-ODS steel tube was isothermally exposed to air at 1200 °C for 10 h to investigate its high-temperature microstructure stability and oxidation behavior. The microstructure and oxide layer were analyzed using electron microscopy and surface analysis techniques. The conclusions could be drawn as follows:

(1) The high density of nanoparticles in pilgered 13Cr-ODS steel tubes successfully delays full recrystallization by pinning grain boundaries. The heterogeneous distribution of these particles allows for localized grain coarsening and a 50% reduction in Vickers hardness.
(2) 13Cr-ODS steel tubes exhibit deformed microstructure, micropores and component segregation and high oxidation rate constant ($K_p = 54.32\ mg^2\ cm^{-4}\ min^{-1}$).
(3) At 1200 °C in air, the 13Cr-ODS steel tubes are insufficient to maintain a protective Cr_2O_3 layer. Instead, the oxidation front is dominated by the formation of a bilayer consisting of a porous, Cr-rich $FeCr_2O_4$ inner spinel and a brittle Fe_3O_4 outer layer. High growth stresses and the development of porosity lead to extensive cracking and spallation of the scale, resulting in an equivalent cladding reacted (ECR) of 27.8% after 2 h.

CRediT authorship contribution statement

Xiao Qin: Writing – review & editing, Writing – original draft, Visualization, Validation, Methodology, Investigation, Formal analysis, Data curation. **Gaoyong Lin:** Writing – original draft, Visualization, Validation, Methodology, Investigation, Formal analysis, Data curation. **Yu Cao:** Writing – original draft, Visualization, Validation, Methodology, Investigation, Formal analysis, Data curation, Conceptualization. **Huiqun Liu:** Writing – review & editing, Writing – original draft, Visualization, Validation, Supervision, Resources, Project administration, Methodology, Investigation, Funding acquisition, Formal analysis, Data curation, Conceptualization.

Declaration of competing interest

The authors declare that they have no known competing financial interests or personal relationships that could have appeared to influence the work reported in this paper.

Acknowledgments

The work presented in this paper was supported by the National Natural Science Foundation of China (5210130601) and the Key Project of Nuclear Safety Advanced Nuclear Technology (2019YFB1901002).

Data availability

Data will be made available on request.

References

[1] S. Ukai, S. Ohtsuka, T. Kaito, Y. De Carlan, J. Ribis, J. Malaplate, Oxide dispersion-strengthened/ferrite-martensite steels as core materials for Generation IV nuclear reactors, Structural Materials for Generation Iv Nuclear Reactors (2017) 357–414. Chapter 10 Elsevier.
[2] V.V. Sagaradze, V.I. Shalaev, V.L. Arbuzov, B.N. Goshchitskii, Y. Tian, W. Qun, S. Jiguang, Radiation resistance and thermal creep of ODS ferritic steels, J. Nucl. Mater. 295 (2–3) (2001) 265–272.
[3] D.T. Hoelzer, J. Bentley, M.A. Sokolov, M.K. Miller, G.R. Odette, M.J. Alinger, Influence of particle dispersions on the high-temperature strength of ferritic alloys, J. Nucl. Mater. 367–370 (2007) 166–172.
[4] R.L. Klueh, P.J. Maziasz, I.S. Kim, L. Heatherly, D.T. Hoelzer, N. Hashimoto, E. A. Kenik, K. Miyahara, Tensile and creep properties of an oxide dispersion-strengthened ferritic steel, J. Nucl. Mater. 307–311 (2002) 773–777.
[5] C.P. Massey, D.T. Hoelzer, P.D. Edmondson, A. Kini, B. Gault, K.A. Terrani, S. J. Zinkle, Stability of a model Fe-14Cr nanostructured ferritic alloy after long-term thermal creep, Scr. Mater. 170 (2019) 134–139.
[6] R.A. Forrest, A. Tabasso, C. Danani, S. Jakhar, A.K. Shaw, Handbook of activation data calculated using EASY-2007, Euratom/ukaea Fusion Association 552 (2009) 399.
[7] E. Aydogan, O. El-Atwani, S. Takajo, S.C. Vogel, S.A. Maloy, High temperature microstructural stability and recrystallization mechanisms in 14YWT alloys, Acta Mater. 148 (2018) 467–481.
[8] I. Hilger, X. Boulnat, J. Hoffmann, C. Testani, F. Bergner, Y. De Carlan, A. Ulbricht, Fabrication and characterization of oxide dispersion strengthened (ODS) 14Cr steels consolidated by means of hot isostatic pressing, hot extrusion and spark plasma sintering, J. Nucl. Mater. 472 (2016) 206–214.
[9] C. Lu, Z. Lu, R. Xie, C. Liu, L. Wang, Microstructure of HIPed and SPSed 9Cr-ODS steel and its effect on helium bubble formation, J. Nucl. Mater. 474 (2016) 65–75.
[10] R. Xie, Z. Lu, C. Lu, Z. Li, X. Ding, C. Liu, Microstructures and mechanical properties of 9Cr oxide dispersion strengthened steel produced by spark plasma sintering, Fusion Eng. Des. 115 (2017) 67–73.
[11] Y. Zhang, B. Liu, Y. Cao, R. Zhang, J. Li, Q. Fang, Y. Liu, Microstructure and mechanical properties of thin-walled ODS ferritic steel tubes fabricated by a near-net forming method, Mater. Sci. Eng. A 899 (2024) 146436.
[12] S.M.S. Aghamiri, T. Sowa, S. Ukai, N. Oono, K. Sakamoto, S. Yamashita, Microstructure and texture evolution and ring-tensile properties of recrystallized FeCrAl ODS cladding tubes, Mater. Sci. Eng. A 771 (2020) 138636.
[13] F.J. Erbacher, S. Leistikow, Zircaloy fuel cladding behavior in a loss-of-coolant accident: a review, Zirconium in the Nuclear Industry (1987).
[14] J.H. Schneibel, C.T. Liu, D.T. Hoelzer, M.J. Mills, P. Sarosi, T. Hayashi, U. Wendt, H. Heyse, Development of porosity in an oxide dispersion-strengthened ferritic alloy containing nanoscale oxide particles, Scr. Mater. 57 (2007) 1040–1043.
[15] M.K. Miller, D.T. Hoelzer, E.A. Kenik, K.F. Russell, Nanometer scale precipitation in ferritic MA/ODS alloy MA957, J. Nucl. Mater. 329–333 (2004) 338–341.
[16] B.A. Pint, I.G. Wright, Oxidation behavior of ODS Fe–Cr alloys, Oxid. Met. 63 (2005) 193–213.
[17] C.P. Massey, P.D. Edmondson, M.N. Gussev, K. Mao, T. Gräning, T.J. Nizolek, D. T. Hoelzer, Insights from microstructure and mechanical property comparisons of three pilgered ferritic ODS tubes, Mater. Des. 213 (2022) 110333.
[18] Y. Zhong, Y. Sun, Y. Du, Z. Zhao, Y. Chen, H.S. Lai, R. Zhang, Low-cycle fatigue behavior and microstructure evolution of ODS steel pipes at high temperatures, J. Mater. Res. Tech. 32 (2024) 1310–1323.
[19] V.S.M. Pereira, T.P. Davis, M.H. Mayoral, A. Kumar, H. Schut, J. Sietsma, Investigation of coarsening of oxide nanoparticles at 1400 K and its effect on the microstructure formation of an ODS Eurofer steel, Mater Charact 185 (2022) 111723.
[20] C. Wagner, Theoretical analysis of the diffusion processes determining the oxidation rate of alloys, J. Electrochem. Soc. 99 (10) (1952) 369.
[21] J. Bischoff, A.T. Motta, Oxidation behavior of ferritic–martensitic and ODS steels in supercritical water, J. Nucl. Mater. 424 (1–3) (2012) 261–276.
[22] D.T. Hoelzer, B.A. Pint, I.G. Wright, A microstructural study of the oxide scale formation on ODS Fe–13Cr steel, J. Nucl. Mater. 283 (2000) 1306–1310.
[23] K. Ding, M.J. Duarte, X. Shen, S. Zhang, J. Li, A. Kostka, X. Fang, Microstructural and micromechanical characterization of intergranular oxidation in Fe-15Cr alloy, Corros. Sci. 225 (2023) 111613.
[24] C.T. Fujii, R.A. Meussner, Oxide structures produced on iron-chromium alloys by a dissociative mechanism, J. Electrochem. Soc. 110 (12) (1963) 1195.
[25] G.C. Wood, D.P. Whittle, The mechanism of breakthrough of protective chromium oxide scales on Fe-Cr alloys, Corros. Sci. 7 (11) (1967) 763–782.
[26] W. Sha, H.K. Bhadeshia, Characterization of mechanically alloyed oxide dispersion-strengthened nickel-base superalloy MA760, Metall. Mater. Trans. A 25 (1994) 705–714.
[27] R.D. Doherty, D.A. Hughes, F.J. Humphreys, J.J. Jonas, D.J. Jensen, M.E. Kassner, W.E. King, T.R. McNelley, H.J. McQueen, A.D. Rollett, Current issues in recrystallization: a review, Mater. Sci. Eng. A 238 (1997) 219–274.
[28] F.J. Humphreys, M. Hatherly, Recrystallization and related annealing phenomena, 3rd. ed., Elsevier, 2017.
[29] T. Ungár, J. Gubicza, G. Ribárik, A. Borbély, Crystallite size distribution and dislocation structure determined by diffraction profile analysis: principles and practical application to cubic and hexagonal crystals, J. Appl. Cryst. 34 (3) (2001) 298–310.
[30] D. Raabe, Recovery and recrystallization: phenomena, physics, models, simulation, Physical Metallurgy (2014) 2291–2397.
[31] S. Ratanaphan, D.L. Olmsted, V.V. Bulatov, E.A. Holm, A.D. Rollett, G.S. Rohrer, Grain boundary energies in body-centered cubic metals, Acta Mater. 88 (2015) 346–354.
[32] C. Zener, Grains, phase, and interfaces: an interpretation of microstructure, Trans. Am. Inst. Min. Metall. Soc. 175 (1948) 15.
[33] Hasegawa, M. Ellingham diagram. In Treatise on Process Metallurgy (2014). Elsevier.

[34] H. Davies, A. Dinsdale, Theoretical study of steam grown oxides as a function of temperature, pressure and p(O2), Mater. High Temp. 22 (1–2) (2005) 15–25.
[35] S.E. Ziemniak, L.M. Anovitz, R.A. Castelli, W.D. Porter, Thermodynamics of Cr_2O_3, $FeCr_2O_4$, $ZnCr_2O_4$, and $CoCr_2O_4$, J. Chem. Thermodyn. 39 (11) (2007) 1474–1492.
[36] W.E. Boggs, R.H. Kachik, G.E. Pellissier, The effects of crystallographic orientation and oxygen pressure on the oxidation of iron, J. Electrochem. Soc. 114 (1967) 32–39.
[37] H.K. Mehtani, M.I. Khan, A. Durgaprasad, S.K. Deb, S. Parida, M.J.N.V. Prasad, I. Samajdar, Oxidation behavior of interstitial free steel: the defining role of substrate crystallographic texture, Acta Mater. 190 (2020) 43–57.
[38] N.B. Pilling, R.E. Bedworth, The oxidation of metals at high temperature, J. Inst. Met. 29 (1923) 529–582.
[39] S. Ukai, Oxide dispersion strengthened steels, Comprehensive Nuclear Materials 4 (2012) 241–271.
[40] G. Hache, H.M. Chung, The history of the LOCA embrittlement criteria, topical meeting on LOCA fuel safety criteria held in aix-en-provence, OECD- NEA (2001) 37–64.
[41] K. Pettersson, H. Chung, M. Billone, T. Fuketa, F. Nagase, C. Grandjean, G. Hache, J. Papin, L. Heins, Z. Hozer, Nuclear fuel behaviour in loss-of-coolant accident (LOCA) conditions, Organisation for Economic Co-Operation and Development (2009).
[42] G. Gaiser, P. Presoly, C. Bernhard, High-temperature oxidation of steel under linear flow rates of air and water vapor-an experimental determined set of data, Metals 13 (5) (2023) 892.
[43] H. Wang, X. Zhou, H. He, L. Guo, Y. Gao, X. Huang, Development of low-Cr wrought FeCrAl cladding alloys and its irradiation tolerance and steam oxidation resistance at 1200 °C, Corros. Sci. 195 (2022) 109998.
[44] D.J. Park, Y.I. Jung, H.G. Kim, J.Y. Park, Y.H. Koo, Oxidation behavior of silicon carbide at 1200 °C in both air and water–vapor-rich environments, Corros. Sci. 88 (2014) 416–422.